Control of nuclear centration in the *C. elegans* zygote by receptor-independent Gα signaling and myosin II

Morgan B. Goulding,[1] Julie C. Canman,[1] Eric N. Senning,[1,2] Andrew H. Marcus,[1,2] and Bruce Bowerman[1]

[1]Institute of Molecular Biology and [2]Department of Chemistry, University of Oregon, Eugene, OR 97403

Mitotic spindle positioning in the *Caenorhabditis elegans* zygote involves microtubule-dependent pulling forces applied to centrosomes. In this study, we investigate the role of actomyosin in centration, the movement of the nucleus–centrosome complex (NCC) to the cell center. We find that the rate of wild-type centration depends equally on the nonmuscle myosin II NMY-2 and the Gα proteins GOA-1/GPA-16. In centration-defective *let-99(−)* mutant zygotes, GOA-1/GPA-16 and NMY-2 act abnormally to oppose centration. This suggests that LET-99 determines the direction of a force on the NCC that is promoted by Gα signaling and actomyosin. During wild-type centration, NMY-2–GFP aggregates anterior to the NCC tend to move further anterior, suggesting that actomyosin contraction could pull the NCC. In GOA-1/GPA-16–depleted zygotes, NMY-2 aggregate displacement is reduced and largely randomized, whereas in a *let-99(−)* mutant, NMY-2 aggregates tend to make large posterior displacements. These results suggest that Gα signaling and LET-99 control centration by regulating polarized actomyosin contraction.

Introduction

Nuclear movement in animal cells can be driven by pulling forces applied to astral microtubules (MTs) emanating from centrosomes bound to the nuclear envelope (Reinsch and Gonczy, 1998). In the one-cell *Caenorhabditis elegans* zygote, asymmetric cleavage is preceded by a series of stereotyped nuclear movements (Fig. 1 A; for review see Cowan and Hyman, 2004). Female and male pronuclei invariably meet in the posterior cytoplasm and move as a unit with the paired centrosomes to the cell center during mitotic prophase; this centration of the nucleus–centrosome complex (NCC) is accompanied by a 90° rotation that aligns the axis of the centrosome pair with the zygote's longer anteroposterior (AP) axis (Albertson, 1984). Shortly after centration and rotation are completed, nuclear envelopes break down, and the mitotic spindle forms.

Laser ablation experiments have revealed that during centration, centrosomes are pulled strongly toward the anterior and weakly toward the posterior (Labbe et al., 2004). These forces are likely transmitted by astral MTs, which extend from each centrosome to the cell cortex and are required for centration and rotation (for review see Cowan and Hyman, 2004). The molecular motors that pull MTs are unknown, as is the molecular basis of their attachment to the cell cortex. Cortically enriched filamentous actin (F-actin) could provide such anchorage; however, disruption of F-actin by cytochalasin D does not prevent NCC centration (Hill and Strome, 1988) or rotation (Hyman and White, 1987), leading to suggestions that cortical F-actin is unlikely to be involved (Grill et al., 2001). The latter conclusion is surprising, as centrosome movement in other systems is clearly F-actin dependent (Euteneuer and Schliwa, 1985).

A related problem is how the forces that drive centration and rotation are spatially regulated. Although spatial regulation is not in principle necessary for centration (Grill and Hyman, 2005), the *C. elegans* zygote is a polarized cell, and an asymmetrically distributed DEP domain–containing protein encoded by the *let-99* gene is required for centration (Rose and Kemphues, 1998; Tsou et al., 2002). The LET-99 protein is enriched in a posterior cortical band coinciding with the initial position of the NCC before centration. In *let-99(−)* mutant zygotes, centration fails, and the NCC undergoes a series of abnormally rapid and extensive oscillatory rocking movements. DEP domains have been implicated in the regulation of heterotrimeric G proteins (Koelle and Horvitz, 1996; Chen and Hamm, 2006),

with LET-99 regulating a redundant pair of Gα subunits called GOA-1 and GPA-16 (Tsou et al., 2003). These two Gα proteins promote forces that pull on spindle pole centrosomes during anaphase in the *C. elegans* embryo (Miller and Rand, 2000; Gotta and Ahringer, 2001; Colombo et al., 2003), as in other systems (for review see Hampoelz and Knoblich, 2004), but their importance for centrosome movement at other stages is unclear. GOA-1/GPA-16 depletion in *let-99(−)* mutant zygotes eliminates NCC rocking, indicating that during wild-type centration, LET-99 restricts excessive force stimulation by Gα signaling (Tsou et al., 2003). Strikingly, GOA-1/GPA-16 depletion also rescues the centration defect in *let-99(−)* mutants, indicating that in the absence of LET-99, inappropriate Gα signaling promotes a net force on the NCC directed away from the cell center toward the posterior pole. However, GOA-1 and GPA-16 have not been shown to influence centration in wild-type zygotes.

In this study, we address two related questions about the control of NCC centration and rotation: the molecular basis of the driving force and the spatial regulation of this force. We show that Gα function is required for wild-type rates of centration and rotation and that the nonmuscle myosin II NMY-2 is required to a similar degree for both processes. Like Gα, actomyosin opposes centration in *let-99(−)* mutants, suggesting that Gα and actomyosin act together to generate a force on the NCC whose direction is determined by LET-99. Finally, we show that cortical NMY-2–GFP aggregates anterior to the NCC move with an anterior bias in wild-type zygotes; this bias is strongly reduced in Gα-depleted zygotes and is reversed in *let-99(−)* mutant zygotes, supporting our conclusion that polarized actomyosin contraction, which is promoted by Gα and spatially directed by LET-99, generates part of the force driving centration and rotation.

Results

The wild-type rate of centration depends on Gα function and myosin II

Centration, the movement of the NCC to the cell center, occurs during mitotic prophase in wild-type one-cell *C. elegans* zygotes (Video 1, available at http://www.jcb.org/cgi/content/full/jcb.200703159/DC1). To determine whether the redundantly acting Gα proteins GOA-1 and GPA-16 contribute to centration, we used RNAi to deplete both simultaneously and measured the rate of NCC movement along the AP axis during centration (see Materials and methods section DIC video microscopy and analysis…). Although not absolutely required for centration, our measurements showed that Gα activity is required for the wild-type rate of centration (Fig. 1 B and Table I). In wild-type zygotes, the speed of the NCC (v_{AP}, plotted as incremental velocity in Fig. 1 B, with peak and mean velocity values in Table I) increased during the first half of centration to a peak value of 7.9 μm/min and a mean value of 6 μm/min followed by a gradual decrease to zero. In contrast to wild-type zygotes, v_{AP} in Gα-depleted zygotes remained relatively constant during centration (Fig. 1 B), and the peak values of v_{AP} were reduced relative to wild type by a factor of approximately two

(4.2 μm/min [*t* test; P < 0.00001] compared with 7.9 μm/min in wild type; Table I). The time-averaged value of v_{AP} was also reduced to 2.0 μm/min compared with 2.9 μm/min in wild type (P < 0.0001). These results suggest that GOA-1 and GPA-16 contribute to an anterior-directed net force on the NCC during centration. The lack of an absolute requirement could reflect a failure to fully deplete these proteins using RNAi or the presence of multiple additive force-generating mechanisms. Further depletion of GOA-1/GPA-16 results in sterility (see Materials and methods section *C. elegans* strains and maintenance), complicating our ability to distinguish between these two explanations (see Discussion).

The molecular basis of force production downstream of Gα signaling during mitotic spindle positioning is unknown. We tested the role of NMY-2, a nonmuscle myosin II required for zygote polarity and cytokinesis (Guo and Kemphues, 1996; Cuenca et al., 2003). A requirement for NMY-2 in centration has not been tested previously because the pronuclei meet near the cell center in most *nmy-2(RNAi)* zygotes (Shelton et al., 1999). To assess the effect of NMY-2 depletion on the centration velocity profile, we examined *nmy-2(RNAi)* zygotes in which fertilization occurred at a site near the oocyte meiotic spindle rather than the typical fertilization site opposite the meiotic spindle (see Materials and methods section *C. elegans* strains and maintenance). In such cases of reversed fertilization, both pronuclei form near one pole and then move together to the cell center (Albertson, 1984; Goldstein and Hird, 1996). In comparison with *NMY-2(+)* zygotes with reversed fertilization, NMY-2–depleted zygotes with reversed fertilization showed substantial reductions in both peak and time-averaged values of v_{AP} (4.8 μm/min and 1.3 μm/min, respectively [P < 0.0001 for both], compared with 10.0 μm/min and 2.6 μm/min in *NMY-2(+)*; Table I). As observed in GOA-1/GPA-16–depleted zygotes, v_{AP} remained at a constantly low level throughout centration in NMY-2–depleted zygotes (Fig. 1 C), and the highest values of v_{AP} were similar to those measured in GOA-1/GPA-16–depleted zygotes (P = 0.08; Table I). Still lower values of v_{AP} were measured in NMY-2–depleted zygotes after normal fertilization, in which the NCC moved only a short distance after pronuclei met near the cell center (Table I).

The reduced NCC velocity in *nmy-2(RNAi)* zygotes could result indirectly from previously documented defects in cell polarity that occur as a result of NMY-2 depletion (Guo and Kemphues, 1996; Shelton et al., 1999). To address this possibility, we examined centration in *par-3(it71)* zygotes, which exhibit extensive polarity defects (Kemphues et al., 1988; Cheng et al., 1995; Etemad-Moghadam and Kemphues et al., 1995; Munro et al., 2004). In *par-3(it71)* mutant zygotes with reversed fertilization (Table I and Fig. 1 C), time-averaged (2.5 μm/min) and peak NCC velocity measurements (6.8 μm/min) were intermediate between wild-type and NMY-2–depleted zygotes (P < 0.0001 for both comparisons; Table I). We also examined NCC movement in normally fertilized *par-3(it71)* zygotes, in which pronuclei met near the center of the zygote, at 58% egg length (EL; compared with 66% EL in wild type). The NCC moved toward the anterior at speeds similar to those observed after reversed fertilization (Table I), invariably moving
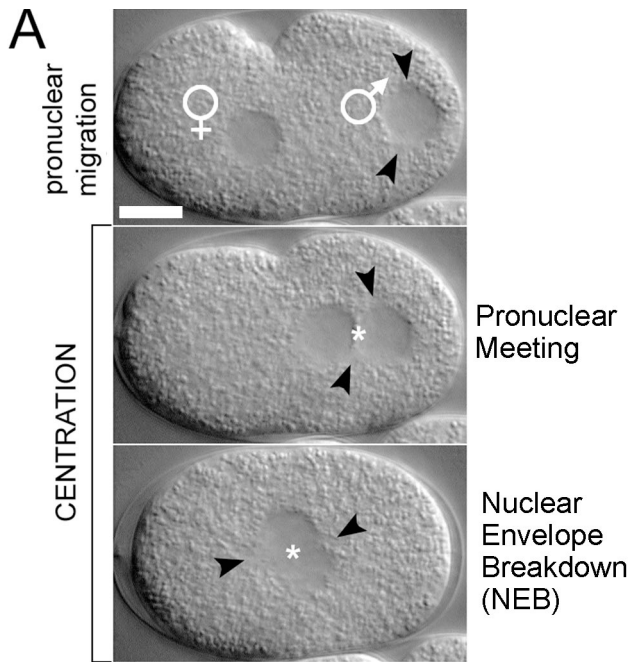
Figure 1. **Gα and myosin II contribute to the rate of centration in wild-type zygotes.** (A) Stereotyped movements of pronuclei and centrosomes in the *C. elegans* zygote. Male and female signs indicate the sperm and egg-derived pronuclei. Centrosomes are marked with arrowheads. The pronuclei initially appear at opposite poles of the cell and migrate toward each other (top). Because the female pronucleus migrates relatively fast from the anterior, pronuclear meeting occurs in the posterior cytoplasm (middle). The joined pronuclei and sperm-derived centrosome pair then move as a unit to the cell center (bottom). To measure rates of centration, we tracked the centroid of the NCC, which is marked here with asterisks. In all figures, zygotes are oriented with the anterior pole to the left. (B) NCC velocity along the AP axis plotted over time in wild-type (WT; $n = 10$ zygotes) and Gα-depleted zygotes ($n = 9$ zygotes). Negative velocities indicate movement from posterior to anterior. (C) NCC velocity along the AP axis plotted over time from pronuclear meeting to NEB ($n = 3$ for each genotype/RNAi treatment) for wild-type, *nmy-2(RNAi)*, and *par-3(it71)* zygotes fertilized near the site of polar body formation (reversed fertilization; see Results for details). Note the longer time axis compared with A. Each point represents a 30-s rolling average derived from measurements made at 10-s intervals; error bars show one SD from the mean of three successive measurements in each zygote. See Table I for peak and mean velocities during centration. Bar, 10 μm.
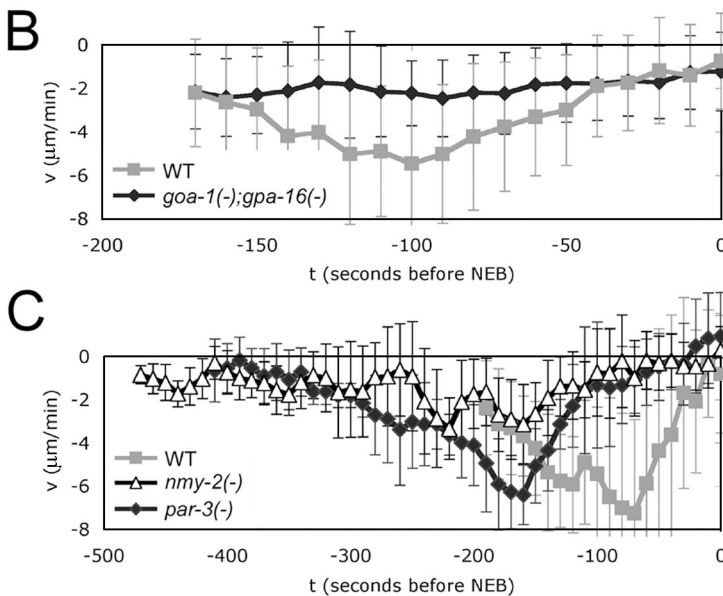
past the center into the anterior cytoplasm (unpublished data). Finally, the rate of NCC movement in *par-3(−)* zygotes was reduced more than twofold by NMY-2 depletion to levels slightly below those measured in NMY-2–depleted wild-type zygotes (Table I), indicating that NMY-2 does not act merely by restricting PAR-3 localization. We conclude that although PAR-3 makes a minor contribution to the rate of centration, the requirement for NMY-2 is at least partially independent of PAR-3 and cell polarity.

We next examined the rate of NCC rotation to determine whether actomyosin and Gα signaling also contribute to this movement. In wild-type zygotes ($n = 30$), the NCC rotated through an angle of $24 \pm 11°$ during the 1-min period preceding nuclear envelope breakdown (NEB; see Materials and methods section DIC video microscopy and analysis…). Similar to the effects on centration, NCC rotation during this time interval was reduced by a factor of approximately two in both GOA-1/GPA-16–depleted and NMY-2–depleted zygotes ($12 \pm 6°$/min for

Table I. **Peak and time-averaged NCC velocities along the AP axis**

Genotype/RNAi	Fertilization site (number of zygotes)	v (peak)[a]	SD	n	v (mean)[b]	SD	n
		μm/min			μm/min		
Wild-type N2	Normal (10)	7.9	1.8	30	2.9	3.2	160
goa-1(−);gpa-16(−)	Normal (8)	4.2	0.9	24	2.0	1.8	156
fer-1(−)	Reversed (3)	10.0	2.1	9	2.6	3.5	93
nmy-2(−)	Reversed (3)	4.8	0.9	9	1.3	1.7	147
par-3(−)	Reversed (3)	6.8	1.4	9	2.1	2.5	119
nmy-2(−)	Normal (6)	3.8	0.9	18	0.5	2.0	199
par-3(−)	Normal (8)	6.2	1.3	24	1.5	2.8	165
par-3(−);nmy-2(−)	Normal (4)	2.5	0.8	12	0.6	1.2	48

The NCC velocities (v) are expressed as absolute rates of NCC displacement toward the anterior pole (micrometers/minute).
[a]v(peak) refers to the mean value of peak NCC velocities between pronuclear meeting and NEB among all zygotes for a given genotype or RNAi treatment (see Materials and methods). The NCC was moving toward the anterior pole for all velocity measurements included in peak values. The number of measurements used to calculate v(peak) is given (n; three measurements/zygote).
[b]v(mean) refers to the mean (time averaged) value of all NCC velocity measurements between pronuclear meeting and NEB for a given genotype or RNAi treatment. The number of measurements used to calculate v(mean) is given (n). Both positive (toward the posterior) and negative (toward the anterior) velocity measurements were included in these calculations.

both; $n = 13$ and $n = 9$, respectively). We conclude that the same actomyosin- and Gα-dependent forces that promote centration also contribute to NCC rotation.

Actomyosin opposes centration in let-99(−) mutant zygotes

To further investigate the relationship between NMY-2, GOA-1/GPA-16, and NCC movement, we altered actomyosin function in let-99(−) mutants, in which an abnormal GOA-1/GPA-16–dependent force prevents centration and causes excess NCC rocking (Tsou et al., 2003). Worms homozygous for a temperature-sensitive allele of let-99 that we isolated and named or513ts (see Materials and methods section C. elegans strains and maintenance) produced zygotes (hereafter referred to as mutant zygotes) that exhibited an absence of centration and excessive NCC rocking at the restrictive temperature of 26°C (Fig. 2, A and B; and Video 2, available at http://www.jcb.org/cgi/content/full/jcb.200703159/DC1). Strikingly, RNAi-mediated depletion of NMY-2 in the let-99(or513ts) mutant rescued centration (Fig. 2, A–C) and reduced NCC rocking by more than fivefold (Fig. 3 and Video 3). In most NMY-2–depleted let-99(or513ts) zygotes ($n = 7$), the pronuclei met posteriorly at a mean position of 63% EL, which is similar to wild-type (66% EL; $n = 10$) and let-99(or513ts) single mutants (67% EL; $n = 8$). NCC position at the time of NEB in the NMY-2–depleted let-99(or513ts) zygotes was significantly further anterior than in let-99(or513ts) single mutants (51% vs. 63% EL; $P < 0.0001$) and was not significantly different from wild type (48% EL; $P = 0.06$). NMY-2 depletion also rescued centration and reduced NCC rocking in another let99(−) mutant, or204ts (unpublished data). We conclude that NMY-2, like GOA-1/GPA-16, is required for the abnormal forces that prevent centration and promote NCC rocking in let-99(−) mutant zygotes.

To further assess the role of myosin II activity in the let-99(−) phenotype, we inactivated the Rho-binding kinase called LET-502, which is required for wild-type levels of NMY-2 activity during cytokinesis and morphogenesis (Piekny et al., 2000; Piekny and Mains, 2002). In embryos from homozygous

let-502(sb106ts);let-99(or513ts) double mutant worms (see Materials and methods section C. elegans strains and maintenance), centration was again rescued (Fig. 2 D), and NCC rocking was strongly reduced (Video 4, available at http://www.jcb.org/cgi/content/full/jcb.200703159/DC1; and unpublished data). Thus, Rho-binding kinase, presumably acting through NMY-2, is required to prevent centration and generate NCC rocking in the absence of LET-99. We also examined let-99(or513ts) zygotes after the depletion of profilin (PFN-1), an F-actin assembly factor that is required for the accumulation of cortical F-actin in the zygote (Severson et al., 2002). In PFN-1–depleted let-99(−) mutant zygotes, the position of pronuclear meeting was highly variable, but, in each case, centration was rescued (Fig. 2 E). The rescue of centration was again accompanied by a marked reduction of NCC rocking compared with the let-99(or513ts) single mutant (Video 5 and unpublished data). We also used RNAi to simultaneously deplete two components of the Arp2/3 complex, another F-actin assembly factor required for cortical stability in the early embryo and for gastrulation but not for the myosin II–dependent processes of cell polarization and cytokinesis (Severson et al., 2002). Depletion of Arp2/3 in let-99(−) zygotes destabilized the cell cortex but did not restore centration (unpublished data), suggesting that the abnormal forces opposing centration in let-99(−) mutant zygotes are mediated specifically by profilin-dependent F-actin in association with NMY-2 but are not affected by a different perturbation of the F-actin cytoskeleton. We conclude that in the absence of LET-99 function, actomyosin-dependent contractile forces oppose centration and contribute to excessive NCC rocking.

Because myosin II activity opposes centration in let-99(−) mutants, we reasoned that overactivating NMY-2 might drive the NCC further toward the posterior pole. To test this prediction, we used RNAi to deplete MEL-11, the C. elegans orthologue of MYPT (myosin phosphatase-targeting subunit), a protein phosphatase that inhibits NMY-2 activity (Piekny et al., 2000). Strikingly, MEL-11 depletion in let-99(or513ts) mutants caused the NCC to move toward the posterior in seven out of eight cases (Fig. 2 F and Video 6, available at http://www.jcb.org/cgi/content/full/jcb.200703159/DC1). To our surprise, the
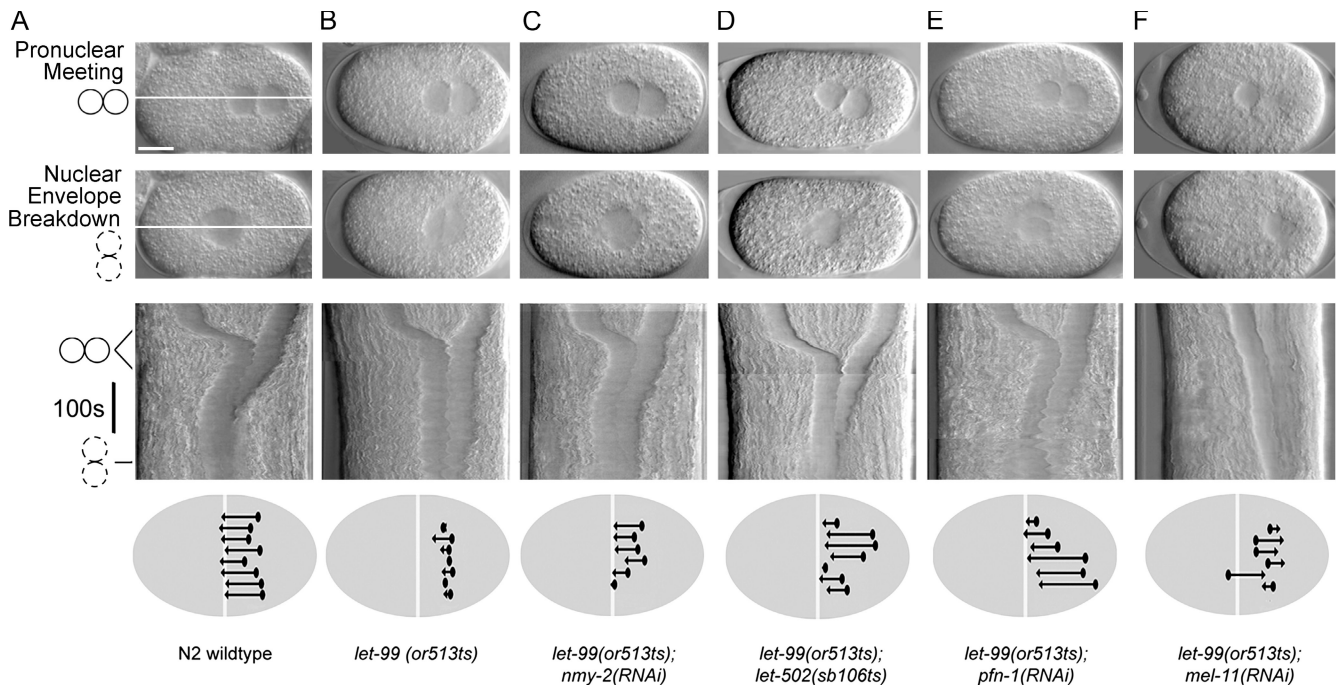
Figure 2. **Centration in *let-99(−)* mutant zygotes is opposed by actomyosin.** (A–F) Still frames (top two rows) show pronuclear meeting and NEB in wild-type and mutant zygotes. Below, kymographs show pronuclear meeting and centration or centration defects in the same zygotes. At the bottom, data from multiple zygotes of each genotype are summarized. Kymographs represent the projection over time of a line of pixels through the midline of the cell (shown in wild-type still frames) and are aligned by the time of NEB. Centration is shown for wild-type (A), is defective in *let-99(or513*ts*)* mutant zygotes (B), is rescued in the *let-99(or513*ts*)* mutant background by depletion of either NMY-2 (C), the Rho-binding kinase LET-502 (D), or the profilin PFN-1 (E), and is reversed by depletion of the inhibitory myosin phosphatase MEL-11 (F). In diagrams at the bottom, line segments show net axial displacement of the NCC from pronuclear meeting (filled ovals) to NEB (arrows) in individual zygotes. Bar, 10 μm.

depletion of MEL-11 also reduced NCC rocking by more than threefold (Fig. 3), suggesting that the amount of rocking is not a simple function of NMY-2 activity.

To summarize, we conclude that although NMY-2 normally acts to promote centration, loss of LET-99 reverses the mechanical output of NMY-2 activity to oppose centration. To account for the suppression of NCC rocking by either the depletion or overactivation of NMY-2, we speculate that the misdirected actomyosin-dependent force in *let-99(−)* mutants is counteracted by an independently generated centration-promoting force and that a balance of roughly equal but oppositely acting forces promotes excess rocking (see Discussion).

Polarized distribution of cortical NMY-2 aggregates during wild-type centration

Seeking to understand how NMY-2 contributes to NCC movement, we used spinning disc confocal microscopy to image cortical NMY-2–GFP in transgenic zygotes during centration. In agreement with previous studies (Munro et al., 2004; Motegi and Sugimoto, 2006), we found the onset of centration to coincide with a sudden reorganization of cortical NMY-2. At the time of pronuclear meeting in wild type, an anteriorly enriched cortical network of relatively large actomyosin bundles is replaced by a more finely reticular F-actin network in which NMY-2 is focused in small, isolated aggregates. Both F-actin and NMY-2 localize most densely to a cap covering the anterior half of the zygote, and a separate, less dense cap of actomyosin also is observed over the posterior pole. The lowest density of

NMY-2 aggregates is consistently found in an intermediate zone (50–75% EL) that encircles the position of the NCC at the beginning of centration. Interestingly, the highest NMY-2 density is always found at the boundary between this intermediate zone and the anterior cap; until a late stage of centration, this myosin-dense ring is several micrometers anterior to the advancing NCC (Fig. 4, Fig. S1, and Video 7, available at http://www.jcb.org/cgi/content/full/jcb.200703159/DC1). Although aggregates appeared to be highly mobile, the overall NMY-2 distribution pattern persisted past the end of centration. Thus, cortical actomyosin is well positioned to play a role in generating forces that pull centrosomes strongly toward the anterior and weakly toward the posterior (Labbe et al., 2004). Although the relative enrichment of NMY-2 in the anterior cap at NEB was slightly reduced in Gα-depleted and *let-99(−)* mutant zygotes (Fig. S1), the significance of this is unclear. Our finding that centration occurs at a near wild-type rate in *par-3(it71)* zygotes, in which NMY-2 aggregates are distributed uniformly throughout the cortex (Munro et al., 2004), suggests that a polarized distribution is unnecessary for the action of NMY-2 in centration. Therefore, rather than focus on the overall distribution of NMY-2, we examined the behavior of individual NMY-2 aggregates for clues to actomyosin's mechanical role.

Wild-type NMY-2 aggregates undergo anteriorly biased movement

If cortical actomyosin is directly involved in generating a pulling force on centrosomes, the mechanism of force generation should
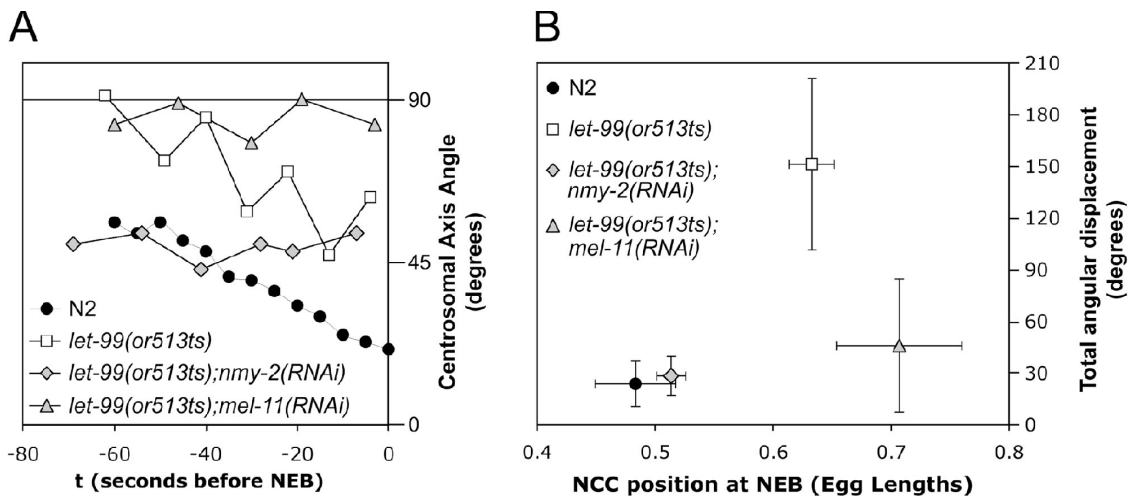
Figure 3. **Effects of NMY-2 inactivation and hyperactivation on centration and NCC rocking in *let-99(−)* mutant zygotes.** (A) NCC rocking in *let-99(or513*ts*)* mutant zygotes is reduced by the depletion of either NMY-2 or the inhibitory myosin phosphatase MEL-11. The angle of the centrosomal axis relative to the AP axis is plotted over time during a 1-min interval before NEB for individual wild-type and *let-99(or513*ts*)* zygotes and for *let-99(or513*ts*)* mutant zygotes depleted of NMY-2 or MEL-11 (in which NCC rocking was partially suppressed). The variation in the angle over time in *let-99(or513*ts*)* zygotes depicts the rocking of the centrosomal axis. This angle varied among individual NMY-2–depleted and MEL-11–depleted *let-99(−)* zygotes but did not change substantially over time in any one zygote (not depicted). (B) NCC position along the AP axis at NEB plotted against total angular displacement of the centrosomal axis during a 1-min interval preceding NEB in wild-type (*n* = 9), *let-99(or513*ts*)* (*n* = 5), and *let-99(or513*ts*)* mutant zygotes depleted of NMY-2 (*n* = 6) or MEL-11 (*n* = 6); error bars show one SD. Total angular displacement refers to the sum of absolute angular displacements in either direction during the 1-min interval.

be reflected by the movements of NMY-2 aggregates. For example, pulling force might be entirely generated by an MT-based motor such as dynein, with actomyosin simply providing cortical anchorage for the motor. In this case, every component of the cortical attachment site, including NMY-2, should tend to move toward the centrosomes if at all. Alternatively (or additionally), NMY-2 itself could itself act as a force generator by pulling the actomyosin cortex and attached MT plus ends away from centrosomes. This model predicts that NMY-2 aggregates in at least some region anterior to the NCC will tend to move away from the NCC during centration. To test these ideas, we used automated particle tracking (Margineantu et al., 2000) to measure displacements of brightly labeled cortical NMY-2 aggregates in the cortical plane of wild-type zygotes (*n* = 10) during the early stage of centration (Fig. 5, A–D; and Video 8, available at http://www.jcb .org/cgi/content/full/jcb.200703159/DC1; see Materials and methods section Particle tracking for details of tracking procedure).

To detect local behaviors of NMY-2 aggregates, we divided the region of the cortical plane from 25 to 75% EL into eight subregions (octants), which were defined with respect to the cell poles and the direction of NCC rotation. Each octant comprised a lateral half of one AP segment with length equal to 12.5% EL (6–7 μm), and the zygotes were oriented such that NCC rotation was clockwise. This convention positioned centrosomes initially near the anterior edge of the posterior-most pair of octants, with the presumptive anterior spindle pole centrosome subsequently swinging through the full breadth of octant g (Fig. 5 E).

We first asked whether NMY-2 aggregate movement in any region of the cortex is directionally biased. For every cortical octant, we obtained the frequency distribution of all displacement sizes at a given time scale projected onto the AP axis (Fig. 6) or the transverse axis (Fig. 7). At short time scales (0.25–2 s),

these distributions resembled smooth Gaussian curves with peaks very close to zero, indicating that random thermal forces influence NMY-2 aggregate movement (unpublished data). At longer time scales (4–16 s), the appearance of directed nonrandom movements along one or both axes became increasingly prominent in some octants (Fig. S2, available at http://www.jcb .org/cgi/content/full/jcb.200703159/DC1).

At the time scale of 12 s, wild-type NMY-2 aggregate displacements throughout much of the cortex were biased toward the anterior (Fig. 6). This bias was evident in the major peaks of displacements in the central octants (b, c, f, and g) near and anterior to the NCC. Large displacements (>1 μm/12 s) were biased toward the anterior on the side of the presumptive anterior spindle pole centrosome (octants e, f, and h) and toward the posterior on the opposite side (octants a–c), suggesting a positive correlation between large displacements of NMY-2 aggregates and the angular displacement of the nearest centrosome.

Anterior movements of NMY-2 aggregates occur independently of mitotic asters

The correlated movements of NMY-2 aggregates and the NCC suggested a mechanical link. To test the possibility that NMY-2 aggregate movement is driven by NCC movement, we blocked centration and rotation by inactivating ZYG-9, a protein required for astral MT stability and, consequently, for centrosome movement. In *zyg-9(or634*ts*)* mutant zygotes (*n* = 8), centration and rotation failed as reported previously (Bellanger et al., 2007), but NMY-2 aggregates in most octants still showed a pronounced anterior bias in peak displacement (Fig. 6). In octants c and g, large displacements in both directions occurred more frequently in the *zyg-9(−)* mutant than in wild type; in octants b and f, large displacements occurred more frequently toward the posterior. We conclude that NMY-2 aggregate motility
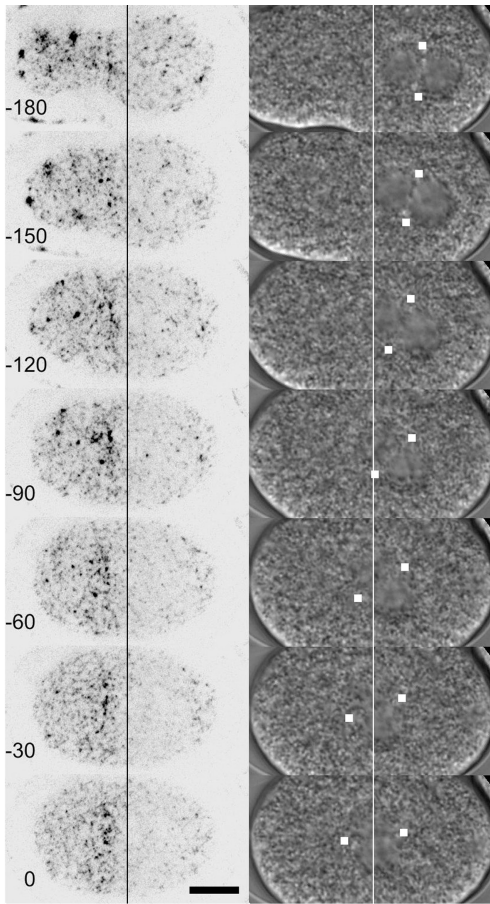
Figure 4. **Dynamic behavior of cortical NMY-2–GFP aggregates during centration.** Time-lapse sequence of cortical NMY-2–GFP in a wild-type zygote, with corresponding DIC images showing centrosomes (white marks). Time in seconds before NEB is indicated. Vertical lines indicate 50% EL. Bar, 10 μm.

shows an intrinsic anterior bias throughout much of the cortex that is independent of aster movement. Interestingly, astral MTs appear to restrict large movements of actomyosin in the equatorial region of the cortex, suggesting that astral MTs and cortical actomyosin are indeed linked.

We also examined NMY-2 aggregate displacements along the transverse axis. In wild type, large displacements (>1 μm/12 s) occurred much more frequently along the transverse axis than along the AP axis (Fig. 7). In every octant, these large displacements were biased in the upward direction, which is coincident with the trajectory of the forward- and upward-moving anterior centrosome. Such biased transverse displacement was strongly reduced in the *zyg-9(−)* mutant, suggesting that transverse aggregate movements are normally stimulated by NCC centration/rotation or by some other function of astral MTs.

Distinct requirements for LET-99 and GOA-1/GPA-16 in NMY-2 aggregate movement

In Gα-depleted and *let-99(−)* mutant zygotes, NMY-2 was similarly localized during prophase to a large, dense anterior cap and a small, sparse posterior cap (Fig. S1, Videos 9 and 10, available
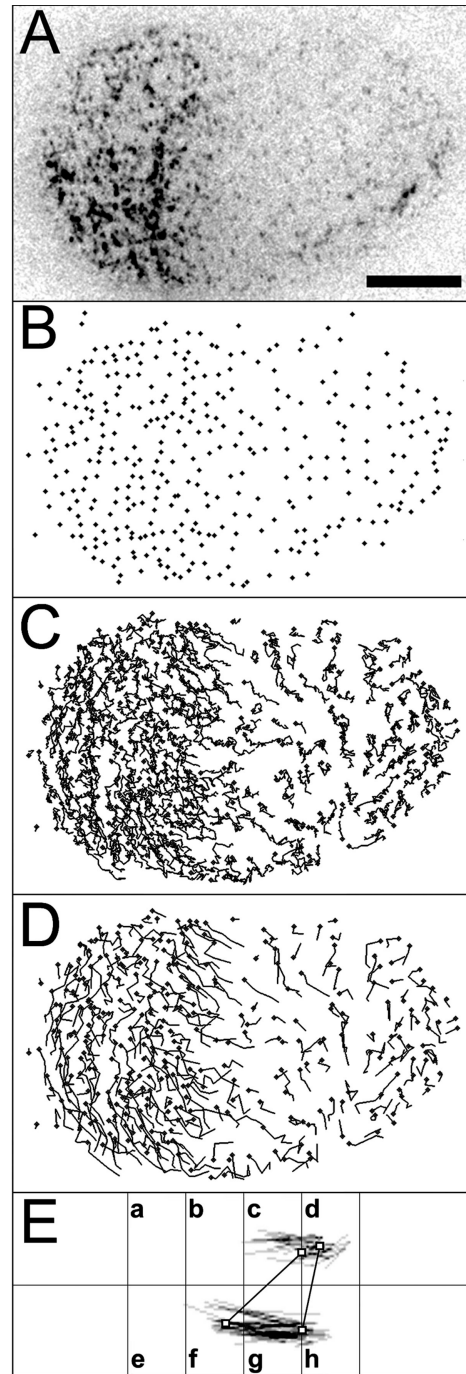

Figure 5. **Using automated particle tracking to measure NMY-2–GFP aggregate displacements.** (A) Cortical NMY-2–GFP imaged for particle tracking in a wild-type zygote 30 s after pronuclear meeting. (B) Features identified from the image in A. (C) Plot of tracks derived from a 60-s 1-Hz video of the same zygote, beginning with the features shown in B. Track ends are marked with diamonds. Every frame is represented in this plot (time scale = 1 s). (D) The same set of tracks, with feature positions plotted every 12th frame (time scale = 12 s). (E) Wild-type centrosome movement in relation to eight regions (octants) defined for regional analysis of NMY-2–GFP aggregate dynamics. Net displacements of wild-type centrosomes during the particle-tracking period are shown by gray lines, summed for 25 zygotes. Mean centrosome positions at the beginning and end of this period are indicated by open squares; a solid line connects the two mean centrosome positions at each time point. Note that the presumptive anterior spindle pole centrosome moves across the full width of octant g. Bar, 10 μm.
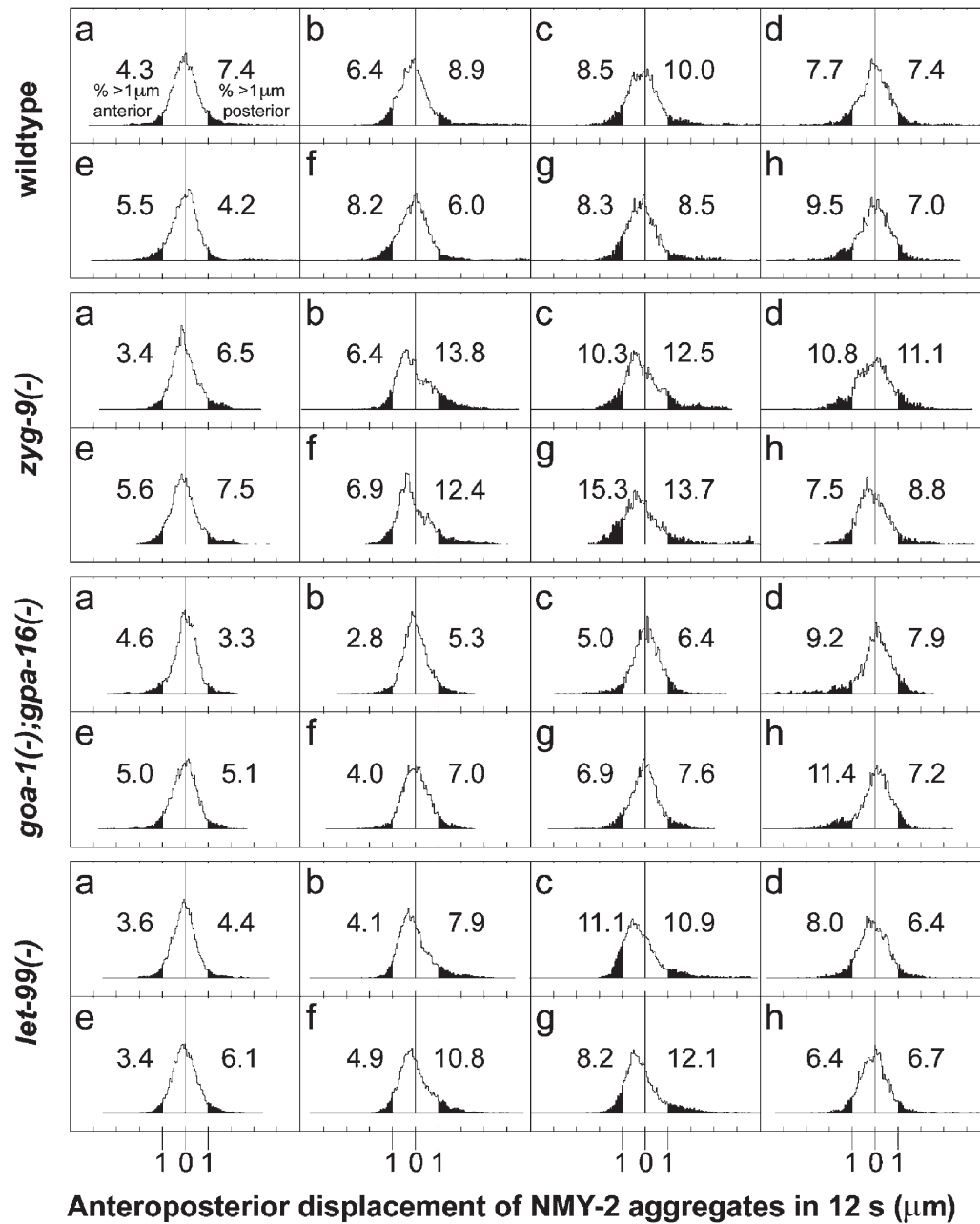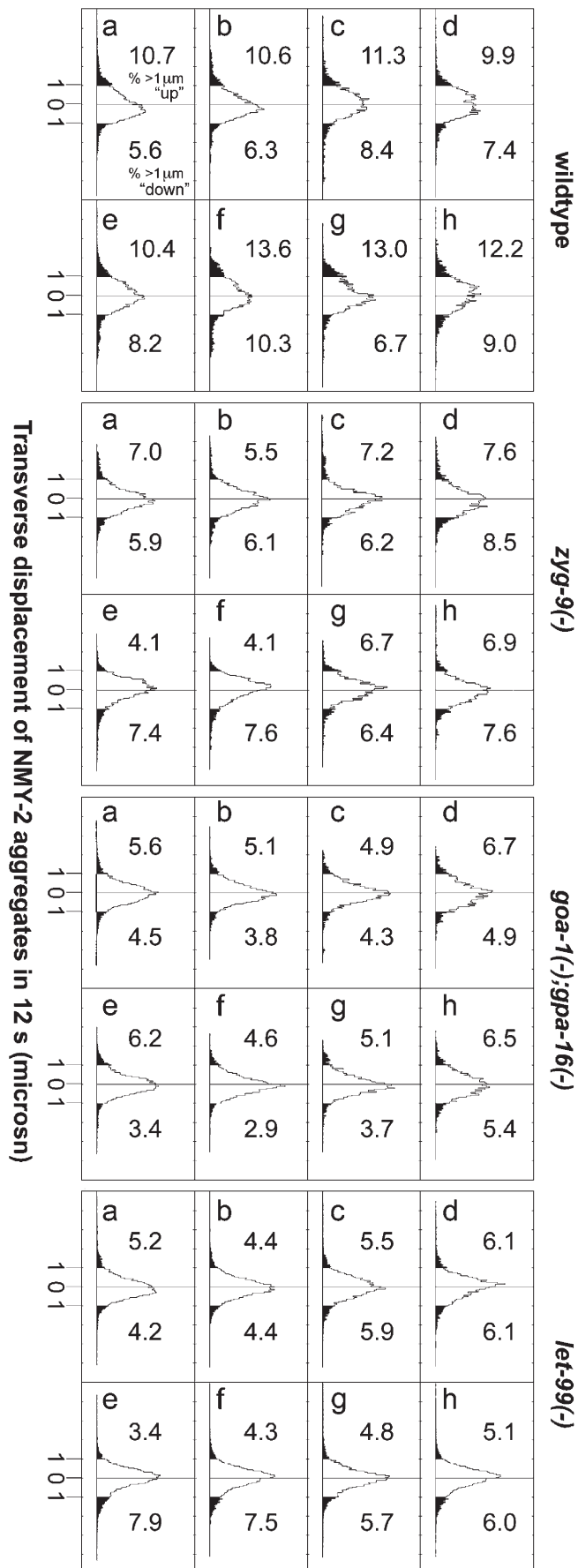
Figure 6. **Distribution of NMY-2 aggregate displacements along the AP axis.** Normalized histograms of AP displacements of NMY-2 aggregates at a time scale of 12 s for each octant of wild-type, *zyg-9(or634*ts*)*, *goa-1(RNAi);gpa-16(RNAi)*, and *let-99(or513*ts*)* zygotes. Tick marks = 1 μm. Displacements of >1 μm are shaded, and the cumulative frequency of >1-μm displacements in each direction is indicated.

at http://www.jcb.org/cgi/content/full/jcb.200703159/DC1; and unpublished data). Although the relative density of NMY-2 in the anterior cap was slightly reduced in both mutants, we thought it was unlikely that LET-99 and Ga exert their disparate influences on centration through similar requirements for polarized NMY-2 enrichment. Instead, a slightly flattened profile of NMY-2 intensity could result in each case from an abnormal pattern of NMY-2 aggregate displacements. Therefore, we examined these displacements in *goa-1;gpa-16(RNAi)* (*n* = 9) and *let-99(or513*ts*)* zygotes (*n* = 11).

In striking contrast to wild type, the AP displacements in cortical regions near and anterior to the NCC in Gα-depleted

zygotes were distributed symmetrically at about zero, suggesting random movement (Fig. 6). However, in the two posterior octants (d and h), the major peaks were biased toward the posterior, indicating that actomyosin movement is not completely randomized by GOA-1/GPA-16 depletion. Also reflecting nonrandom behavior, large displacements (>1 μm/12 s) were prominently biased toward the NCC in regions both to its anterior (b and f) and its posterior (d and h; see Discussion).

A different abnormal pattern of biased displacement along the AP axis was detected in *let-99(−)* zygotes (Fig. 6). In all four central octants (b, c, f, and g), displacements showed a characteristically abnormal profile, with peaks offset further

Transverse displacement of NMY-2 aggregates in 12 s (microsn)

wildtype

a 10.7 % >1μm "up"	b 10.6	c 11.3	d 9.9
5.6 % >1μm "down"	6.3	8.4	7.4
e 10.4	f 13.6	g 13.0	h 12.2
8.2	10.3	6.7	9.0

zyg-9(-)

a 7.0	b 5.5	c 7.2	d 7.6
5.9	6.1	6.2	8.5
e 4.1	f 4.1	g 6.7	h 6.9
7.4	7.6	6.4	7.6

goa-1(-);gpa-16(-)

a 5.6	b 5.1	c 4.9	d 6.7
4.5	3.8	4.3	4.9
e 6.2	f 4.6	g 5.1	h 6.5
3.4	2.9	3.7	5.4

let-99(-)

a 5.2	b 4.4	c 5.5	d 6.1
4.2	4.4	5.9	6.1
e 3.4	f 4.3	g 4.8	h 5.1
7.9	7.5	5.7	6.0

toward the anterior than in wild type. In three of these four central octants, however, the largest displacements (>1 μm/12 s) were strongly biased toward the posterior (to a more subtle degree, this bias was also present in the two anterior-most octants, a and e). An abnormally polarized trend in large displacements occurred in octants b and f: large displacements occurred more frequently toward the posterior and more rarely toward the anterior compared with wild type. The resulting degree of asymmetry was beyond any found in wild-type or Gα-depleted zygotes, although similar profiles of anteriorly biased small and posteriorly biased large displacements were found in *zyg-9(−)*.

Surprisingly, the inactivation of LET-99 caused a striking reduction in both the magnitude and directional bias of transverse displacements (Fig. 7). Similarly narrow and symmetrical displacement profiles were measured in most regions of Gα-depleted zygotes, with the two posterior octants again showing distinctively nonrandom trends. Thus, both GOA-1/GPA-16 and LET-99 seem to play essential roles in generating the directionally biased movement of NMY-2 aggregates along the transverse axis.

Time-dependent mobility of NMY-2 aggregates is distinctly altered by inactivating LET-99 or GOA-1/GPA-16

To better understand the mechanics of NMY-2 aggregate movement and its control by Gα and LET-99, we next measured the total mobility of NMY-2 aggregates as a function of time scale. In general, the tendency of a particle to move from its initial position over time reflects the forces it experiences in its local environment, including both active transport and constraining forces. Such forces may act at distinct time scales, leading to time-dependent variation in particle mobility. For a population of particles, this can be measured as the time-dependent mean-squared displacement (MSD; see Materials and methods section Particle tracking). Changes in the character of the movement are reflected by changes in the slope of the MSD as a function of time scale; this slope is proportional to the diffusion coefficient (here termed mobility) of the aggregates and reflects the cumulative contributions of random thermal forces, active transport, and constraining forces acting over a given range of time scale. Active transport, which is driven by molecular motors or cytoskeletal assembly dynamics, is expected to generate a positive change in MSD (increased aggregate mobility) over the range of time scale in which it produces directed motion. On the other hand, opposition to such transport will negatively affect aggregate mobility over an independent range of time scales.

For each population of aggregates, we measured the projection of the MSD onto the AP and transverse axes. In all wild-type and mutant/RNAi conditions, mobility in some octants increased and/or decreased over time scales ranging from 4 to 16 s (Fig. 8), suggesting that diverse factors or conditions locally modify NMY-2 aggregate mobility. Interestingly, throughout

Figure 7.   **Distribution of NMY-2–GFP aggregate displacements along the transverse axis.** Histograms of aggregate displacements projected on the transverse axis at a time scale of 12 s, with >1-μm displacements shaded and labeled as in Fig. 6.

Figure 8. Mobility of NMY-2–GFP aggregates varies in a spatial pattern that depends on GOA-1/GPA-16 and LET-99. One-dimensional MSD of NMY-2–GFP aggregates plotted over time for wild-type, *let-99(or513*ts), and *goa-1 (RNAi);gpa-16(RNAi)* zygotes. MSD values are shown as open diamonds (red, displacements projected on the AP axis; blue, projected on the transverse axis). Solid lines are extrapolated from MSD values at time scales of 1 and 2 s; their slopes (with values shown) indicate short-time aggregate mobilities.
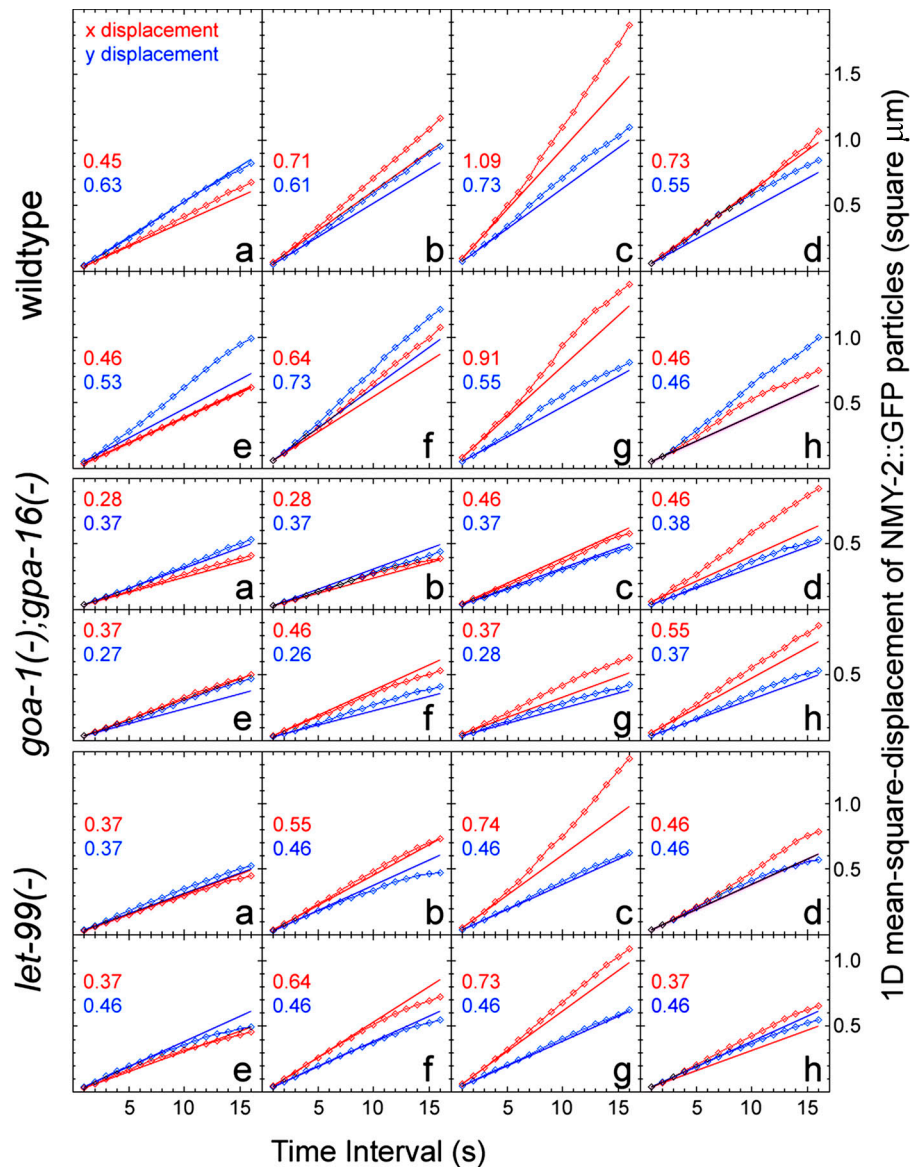
most of the regions examined, mobility over time scales of 1–2 s was higher in wild type than in the corresponding octants of Gα-depleted or *let-99(−)* zygotes, suggesting that wild-type aggregates move relatively fast and/or in a more directed manner at these short time scales. At longer time scales as well, wild-type NMY-2 aggregates in most regions of the cortex showed relatively high AP mobility, which is consistent with a normal predominance of directed transport that is lacking or constrained in the absence of Gα or LET-99.

Both short-time and long-time mobilities varied substantially with position, being highest in wild type near the NCC (octants c and g) and lowest in the anterior octants (a and e), with more than a twofold difference between these regions. In general, mobility along the AP axis was markedly diminished in Gα-depleted zygotes, with the exception of the most posterior region, where asymmetric displacement peaks had been observed (Fig. 6). Together, these data suggest that GOA-1/GPA-16 are required for directed movement in anterior regions, but only for the spatial regulation of directed movement in the posterior.

In *let-99(−)* zygotes, an interesting asymmetry was detected: in anterior regions, mobility did not increase over time but rather decreased over time scales of 10–15 s. This time-dependent decrease was expected as a reflection of oscillatory cortical flows that occur in approximate synchrony with NCC rocking (unpublished data). Strikingly, mobility in posterior regions of *let-99(−)* zygotes tended to increase over time, showing only a slight decrease at the time scale of NCC oscillation. This regional difference in aggregate mobility could account for the abnormal distribution of NMY-2–dependent forces that act on the NCC in *let-99(−)* mutant zygotes (see Discussion).

Transverse mobility increased over time in most regions of the wild-type cortex, but the pattern of regional variation was roughly opposite that of AP mobility, indicating local preferences for aggregates to move along one axis or the other (Fig. 8). Strikingly, time-dependent mobility increases along the transverse axis were largely absent in both *goa-1(−);gpa-16(−)* and *let-99(−)* zygotes. Together with the symmetrically distributed displacements along the transverse axis in both conditions
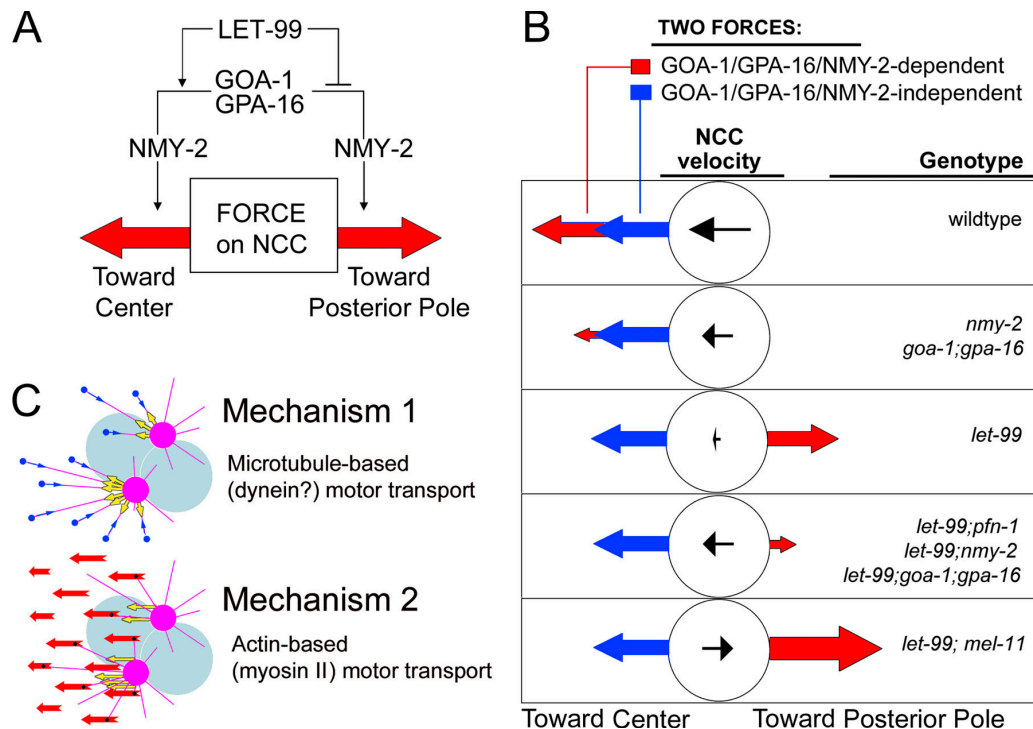
Figure 9. **Forces on the NCC during centration.** (A) We hypothesize that GOA-1/GPA-16 and NMY-2 contribute to a force-generating mechanism that can promote NCC movement in opposite directions, with LET-99 favoring the anterior direction. (B) Based on the results of this and previous studies, we speculate that two independent forces drive NCC movement: a Gα- and NMY-2–dependent force (depicted in A) that is oriented by LET-99 (red arrows) and another force independent of these factors (blue arrows). NCC velocity depends on the sum of the two forces. This model accounts for the effects of varying NMY-2 activity in a let-99(–) mutant background. (C) Cartoon of two proposed mechanisms driving centration, with arrows indicating force vectors; yellow arrows represent forces on centrosomes. Mechanism 1: fixed MT-based motors (blue arrows) pull cortical sites toward MT minus ends. Mechanism 2: NMY-2 acts as a force generator (red arrows) by pulling MT attachment sites away from centrosomes in the cortical plane. In wild type, both mechanisms act in parallel. In Gα-depleted zygotes, only mechanism 1 acts. In let-99(–) zygotes, mechanism 1 acts normally, whereas the force vectors of mechanism 2 are spatially reversed.

(Fig. 7), this result suggests that the directionally biased active transport of NMY-2 aggregates along the transverse axis depends on both GOA-1/GPA-16 and LET-99.

Discussion

We have shown that the Gα proteins GOA-1/GPA-16 and the myosin II NMY-2 act similarly to promote NCC centration and rotation in wild type and to oppose centration and provoke excessive NCC rocking in *let-99(−)* mutants. In addition to NMY-2, the F-actin assembly factor PFN-1 and the Rho-binding kinase LET-502, which activates NMY-2 by phosphorylating its regulatory light chain, are also required to prevent centration in the absence of LET-99. Moreover, depletion of the inhibitory myosin II light chain phosphatase MEL-11 in a *let-99(−)* mutant promotes posterior movement of the NCC. Based on these findings, we propose that the Gα proteins, acting either through or in parallel to myosin regulatory light chain phosphorylation, activate an actomyosin-dependent force that promotes NCC movement and that the direction of this force is regulated by LET-99 (Fig. 9 A). Our findings also suggest that the actomyosin-dependent force acts in parallel with a separate, unidentified centration-promoting force that is independent of actomyosin, Gα, and LET-99. Finally, we have shown that elements of the actomyosin cortex undergo intrinsically polarized movement that could directly generate a

pulling force on centrosomes, and we propose that Gα and LET-99 act by regulating this movement.

Our findings challenge the view that actomyosin is not required for centrosome movement in the early *C. elegans* embryo (see Introduction). Analysis of direct roles of actomyosin in centrosome positioning in the *C. elegans* embryo has previously been complicated by an earlier requirement for the polarization of cortical PAR (partitioning) proteins, which, in turn, are thought to act upstream of Gα and LET-99 to control centrosome movement (Colombo et al., 2003; Tsou et al., 2003). However, F-actin appears to play PAR-independent roles in the Gα-dependent processes of anaphase spindle pole flattening and NCC rotation (Severson and Bowerman, 2003). Our finding that NMY-2 promotes centration in *par-3(it71)* zygotes likewise indicates a direct role for actomyosin and further suggests that centration is independent of cortical polarity, as neither NMY-2 nor LET-99 is asymmetrically distributed in *par-3(it71)* zygotes at this stage (Tsou et al., 2002; Munro et al., 2004). In contrast, NCC rotation appears to depend on PAR-3 as well as on Gα, LET-99, and NMY-2 (Tsou et al., 2002).

Two force-producing pathways promote centration in the *C. elegans* zygote

Centration was slowed but never completely blocked by the depletion of GOA-1/GPA-16 or NMY-2 (see Materials and

methods section *C. elegans* strains and maintenance). Considering this result with prior evidence that centration can occur independently of F-actin (Hill and Strome, 1988), we propose that wild-type centration results from the additive effects of two parallel force-generating mechanisms, one of which is promoted by Gα/actomyosin and spatially oriented by LET-99. In this scenario, the near-zero net axial movement of the NCC observed in *let-99(−)* mutants can be explained as the result of a balanced conflict between two opposing forces that normally cooperate to drive centration (Fig. 9 B).

If one or both of the opposing forces in *let-99(−)* varies with centrosome position and velocity, the conflict between them might drive excessive NCC rocking (Grill et al., 2005; Pecreaux et al., 2006; Kozlowski et al., 2007), and this rocking could be reduced by tipping the balance of force in either direction. We were indeed able to suppress NCC rocking by either reducing or increasing the posterior-directed actomyosin-dependent force in a *let-99(−)* mutant. Interestingly, simulation of wild-type anaphase centrosome oscillations (which occur with roughly the same period as the prophase oscillations in *let-99(−)* zygotes) shows that rocking can be reduced to zero by either increasing or decreasing a cortical pulling force (Pecreaux et al., 2006).

Wild-type NMY-2 aggregate dynamics suggest that cortical actomyosin acts as a force generator

Based on the behavior of wild-type NMY-2–GFP aggregates, we can distinguish between different models for the role of actomyosin in centration. Several current models of centrosome movement in the *C. elegans* embryo posit that force generators bind and effectively shorten astral MTs while anchored to fixed cortical sites (Fig. 9 C, mechanism 1; for review see Cowan and Hyman, 2004; Grill and Hyman, 2005; Kozlowski et al., 2007). Our finding that NMY-2–GFP aggregates anterior to the NCC move with an aster-independent anterior bias suggests instead that a pulling force may be generated by the intrinsic motility of MT attachment sites within the cortical plane (Fig. 9 C, mechanism 2). Such actomyosin-based motility of cortical sites indeed appears to move asters in yeast (Hwang et al., 2003) and mammalian cells (Rosenblatt et al., 2004). However, we measured peak centrosome velocities during centration that far exceed the highest rates of NMY-2– GFP aggregate movement. We speculate that both types of pulling mechanisms (attachment site motility and tethered MT shortening) may operate in tandem so that the resulting forces are coupled. Alternatively, rapid MT binding and release by NMY-2 aggregates could ratchet them toward MT minus ends, and many such small pulling movements could generate a large summed force on the NCC.

Remarkably, an anterior bias in aggregate displacement was not found in the most anterior cortical regions but only in regions a short distance anterior to the NCC. Any pulling force exerted on the NCC by these biased movements would therefore be predicted to diminish toward the end of centration. This prediction is consistent with the sinusoidal NCC displacement profile observed in wild type (Kimura and Onami, 2005), corresponding to the bell-shaped velocity profile shown in Fig. 1.

As the velocity increase during early centration depends on NMY-2, it is plausible that the local regulation of polarized cortical contraction acts to generate a position-dependent pulling force on centrosomes.

Roles of GOA-1/GPA-16 and LET-99 in cortical NMY-2 aggregate motility

Given the similar requirements of NMY-2 and GOA-1/GPA-16 for promoting centration in wild-type zygotes and opposing it in *let-99(−)* mutants, we hypothesized that Gα signaling influences actomyosin contractility to promote centration in wild-type zygotes. Indeed, the loss of anteriorly biased NMY-2–GFP aggregate movement in cortical regions anterior to the NCC is consistent with a role of Gα signaling in directing biased actomyosin contraction. Gα is not simply required for NMY-2 aggregate movement, however, as directed movement was evident in octants near and posterior to the NCC in Gα-depleted zygotes. An alternative mechanism of Gα action is suggested by the bidirectional bias of large AP displacements toward the NCC in *goa-1(−);gpa-16(−)* zygotes. We speculate that Gα signaling might induce the relaxation of actomyosin in the vicinity of asters, allowing long-range contractile flow toward distal cortical regions. Supporting this model, GOA-1/GPA-16 and their positive regulator GPR-1/2 are also required for the spindle poles to transmit a cytokinesis-promoting signal during anaphase, and GPR-1/2 is enriched at this stage in the polar cortex, where relaxation is thought to occur (Bringmann et al., 2007). Other Gα proteins are known to affect actomyosin assembly and contraction through regulation of the small G proteins Rho and Rac (Sugimoto et al., 2003; Rogers et al., 2004), raising the possibility that GOA-1/GPA-16 may influence aster-associated actomyosin through the local regulation of one of these pathways.

Because LET-99 has been shown to negatively regulate Gα-dependent forces that promote NCC rocking (Tsou et al., 2003), we expected LET-99 inactivation to also perturb NMY-2–GFP aggregate dynamics, but in a manner distinct from the effect of GOA-1/GPA-16 depletion. Indeed, NMY-2–GFP aggregates in *let-99(−)* mutant zygotes exhibited a characteristic pattern of abnormal movements throughout a large region of the cortex. In contrast to the anterior direction of large displacements near the forward-moving centrosome in wild type, the largest displacements near and anterior to the NCC in *let-99(−)* zygotes were directed toward the posterior. Thus, LET-99 appears to reverse the net directional force acting on a fast-moving subpopulation of cortical NMY-2–GFP aggregates near the NCC. If these aggregates bind to astral MTs, their behavior in the *let-99(−)* mutant could explain the reversal of the actomyosin-dependent force that promotes centration in wild-type zygotes. Interestingly, posteriorly biased large displacements were similarly observed in *let-99(−)* zygotes near the NCC, where active transport predominated, and anteriorly adjacent to this region, where constraining forces predominated. This relationship suggests that NMY-2–GFP aggregates in these two regions are mechanically linked and that polarized actomyosin contraction in the posterior cortex of *let-99(−)* zygotes exerts a pulling force on the anterior cortex.

It is intriguing that the transverse movement of NMY-2 aggregates was greatly reduced in both *zyg-9(−)* and *let-99(−)* mutants. As this movement requires the normal activity of astral MTs (absent in *zyg-9(−)*), we expected it instead to be increased by the hyperactive aster movement in *let-99(−)*. We speculate that signaling from astral MTs may induce the directed movement of actomyosin through a mechanism that operates on a relatively long time scale compared with that of NCC rocking. Such a positive feedback effect on actomyosin movement could play an important role in generating smooth and directed centrosome movement during centration. To further elucidate how actomyosin interacts with astral MTs to drive centrosome movement, it will be interesting to examine the correlated trajectories of astral MTs and associated NMY-2 aggregates in doubly labeled zygotes.

Materials and methods

C. elegans strains and maintenance

N2 Bristol was used as the wild-type strain and was maintained according to Brenner (1974). Alleles listed by chromosome number were used as follows: *fer-1(hc1*ts*), let-502(sb106*ts*)* I; *zyg-9(or634*ts*)* II; *dpy-19(e1259), glp-1(q339), let-99(or204*ts*), let-99(or513*ts*), lon-1(e185), par-3(it71)* III; *unc-17(e245)* IV; *him-5(e1467)* V; and *lin-2(e1309)* X. *par-3(it71)* mutant embryos were obtained by picking long adults from the strain KK571 (*lon-1(e185) par-3(it71)/qC1[dpy-19 (e1259) glp-1(q339)]* III). To visualize cortical NMY-2–GFP, we used the strain JJ1473 (*unc-119(ed3)* III; *zuIs45[nmy-2–NMY-2–GFP+unc-119(+)]* V). NMY-2–GFP localization throughout early cleavage in live embryos is indistinguishable from the immunolocalization of endogenous NMY-2 (Munro et al., 2004).

*let-99(or204*ts*)* and *let-99(or513*ts*)* were isolated in screens for temperature-sensitive embryonic-lethal mutations affecting early cell divisions (Encalada et al., 2000). Both were outcrossed to N2 males through six generations before phenotypic analysis. In both mutants, the defective centration phenotype was strongly expressive immediately after shifting worms from 15°C to room temperature, suggesting that the mutant proteins rapidly inactivate. *or204*ts and *or513*ts mutant worms were maintained at 15°C and shifted to 26°C for at least 1 h before beginning experiments. Broods of embryos produced by hermaphrodites homozygous for either *or204*ts or *or513*ts were nearly 100% viable at 15°C and >99% lethal at 26°C. Both alleles were mapped to linkage group IV by mating with strains carrying visible mutations. *or204*ts is strictly recessive: 914/945 (97%) embryos from heterozygotes grown at 26°C hatched. *or513*ts may be weakly dominant: 818/898 (91%) embryos from heterozygotes grown at 26°C hatched. *or204*ts failed to complement a known recessive and nonconditional *let-99* allele, *or81* (Tsou et al., 2002), and further failed to complement *or513*ts. To identify the molecular lesions in *or204*ts and *or513*ts, genomic DNA encompassing the K08E7.3 (*let-99*) locus was amplified from each mutant by PCR using primer sequences not found in the paralogous locus F55H2.4 (*lrg-1*). Sequences from pooled PCR reactions were obtained using a genetic analysis sequencer (CEQ 800; Beckman Coulter) at the University of Oregon Sequencing Facility and were compared with published wild-ype sequences as well as the background strain used for mutagenesis, CB1309 (*lin-2(e1309)* X) Sequence analysis revealed that *or204*ts carries two missense mutations at the *let-99* locus: a T→A transition that converts leucine 409 to histidine and a G→A transversion that converts arginine 515 to histidine. *or513*ts also carries two missense mutations in *let-99*: a G→A transversion that converts aspartate 371 to asparagine and a T→C transversion that converts methionine 405 to threonine. None of these four mutations was present in CB1309. The phenotypes of *or204*ts or *or513*ts are indistinguishable from other *let-99(−)* mutants described previously (Rose and Kemphues, 1998).

A double mutant strain of the genotype *let-502(sb106*ts*)* I;*let-99 (or513*ts*)* IV was constructed by mating *let-502(sb106*ts*)* males with *unc-17 (e245) let-99(or513*ts*)* hermaphrodites. The *let-502* mutation confers a visible phenotype with fewer oocytes than normal present in the hermaphrodite uterus; from F2 self-progeny that were Unc with few oocytes, we recovered a strain homozygous for both *sb106*ts and *or513*ts. Double mutant worms were maintained at the restrictive temperature of 26°C for at least 6 h before collecting embryos. We confirmed the presence of the

*or513*ts mutation by outcrossing the double mutant strain with N2 males to recover an *unc-17 or513*ts strain that was wild type at the *let-502* locus.

To obtain wild-type embryos with reversed fertilization, *fer-1(hc1*ts*)* hermaphrodites were shifted to the restrictive temperature of 26°C for several hours and were mated with wild-type males (Goldstein and Hird, 1996).

All RNAi was performed by feeding worms on lawns of RNase III–deficient *Escherichia coli*–expressing double-stranded RNA from inducible promoters. Most bacterial strains were obtained from the library of Kamath et al. (2003) and distributed by Geneservice Ltd. The *goa-1*;*gpa-16* double RNAi feeding strain was provided by P. Gonczy (Swiss Institute for Experimental Cancer Research, Lausanne, Switzerland; Colombo et al., 2003). Bacterial lawns were grown overnight at 37°C on feeding RNAi plates containing 1 mM IPTG + 75 μg/ml ampicillin (Kamath et al., 2003) from ∼200 μl of a twofold concentrated stationary-phase liquid culture (uninduced) and were stored for up to 2 wk at 4°C. Worms were transferred to feeding RNAi plates as suspensions of unfed L1 hatchlings and grown at 15°C until adulthood. With the exception of *mel-11*, all RNAi treatments caused a proportion of animals to become sterile and produce no eggs. In cases in which treatment from L1 produced sterility, worms were plated at later stages of development. All RNAi treatments were predicted to affect phenotypic traits other than NCC movement; the presence of these phenotypic markers in zygotes or their siblings was used to assess the efficacy of gene inactivation. For example, to ensure that NMY-2 was strongly depleted, we collected data only from zygotes showing severe defects in the NMY-2–dependent processes of cytokinesis and interphase cortical contractility. In the case of *goa-1*;*gpa-16* double RNAi, zygotes were used whose older siblings showed large multinucleate cells, which is a result of cytokinesis defects during late cleavage that indicates the effective depletion of both GOA-1 and GPA-16.

DIC video microscopy and analysis of NCC movement

Zygotes were dissected out in M9 salts, placed on 3% agarose pads, and overlaid with a coverslip, under which was placed enough M9 to delay evaporation from the agar pad. For Nomarski differential interference contrast (DIC) microscopy, 63× 1.4 NA oil immersion objectives (Carl Zeiss MicroImaging, Inc.) were used with microscopes (Axioskop; Carl Zeiss MicroImaging, Inc.). DIC images were collected at room temperature (23 ± 1°C) at frame rates of 0.1–2.0 Hz using a digital video camera (307,200 pixels^2; CCDX; Dage-MTI) connected to a frame-grabber card controlled by a computer (G4; Macintosh). The frame-grabber software was Image 1.62 (Scion) run on an OS9 operating system (Macintosh). These image sequences were collected as TIFF stacks and analyzed using ImageJ (National Institutes of Health [NIH]) and Excel (Microsoft). Image stacks were rotated to align the zygote's AP axis horizontally with anterior to the left. The NCC position, relative to the zygote's anterior pole at the time of NEB, was tracked at 10-s intervals beginning just before pronuclear meeting and terminating at NEB. The center of the NCC (midpoint between the diametrically opposed centrosomes) was approximated by eye. NCC velocity was calculated for each 10-s interval. The mean velocity and SD for each genotype/RNAi treatment were computed for the period between pronuclear meeting and NEB. To estimate peak velocities, incremental velocity measurements for each zygote of a given genotype/RNAi treatment were sorted in descending order; the three highest values obtained for each zygote were selected, and the mean of these values was computed for all zygotes. Net NCC rotation in wild-type, *nmy-2(RNAi)*, and *goa-1 (RNAi)*;*gpa-16(RNAi)* zygotes was measured during the 60 s preceding NEB. NCC angular position was measured as the angle of a line connecting the two centrosomes relative to the AP axis, and the change in this angle over the 60-s period was calculated. NCC oscillations in *let-99(−)* single and double mutants were also measured during the 60 s preceding NEB, when the NCC in *let-99(−)* single mutants is abnormally rotating in place. At each reversal of NCC rotation, angular position was measured as the angle of a line connecting the two centrosomes relative to the AP axis. To compare any two sets of measurements, we used the *t* test (two-tailed, assuming unequal variance).

Fluorescence microscopy and analysis of NMY-2–GFP localization

All fluorescence imaging was performed by spinning disc confocal microscopy. NMY-2–GFP was excited using a 300-mW argon laser (Dynamic Laser; Solamere Technology Group) coupled via optical fiber to a spinning disc confocal attachment (Yokogawa; PerkinElmer). The spinning disc head was mounted onto a side port of an inverted fluorescence microscope (TE2000U; Nikon), which was used with either a 60× or 100× plan Apo DIC 1.4 NA objective (Nikon). Transmitted light was shuttered using a custom adapted shutter (Uniblitz; Applied Scientific Instrumentation), whereas

excitation and emission light was filtered using two filter wheels (MetalTek) controlled by a driver (Lambda 10–2; Sutter Instrument Co.). In the case of DIC imaging, the emission was filtered according to polarization; for GFP fluorescence imaging, the emission was filtered using a 505-nm-long pass filter (Z485LP; Chroma Technology Corp.). Focusing of the objective was controlled by a XYZ automated stage (PZ-2000; Applied Scientific Instrumentation) with a piezo z-axis top plate. All image acquisition was controlled by MetaMorph imaging software version 6.2r6 (Molecular Devices). Zygotes were collected and mounted as for DIC microscopy except that the slide was warmed to 26°C using a Bionomic cell (BC-300W; 20/20 Technologies).

To quantitate cortical NMY-2–GFP intensity, we imaged the entire thickness of the zygote cortex in a z-series of eight images 0.2 μm apart and used ImageJ to make a two-dimensional projection by summing the signal at each point. We selected a rectangular area corresponding to the median 50% of the zygote (25% egg width on each side of a line corresponding to the AP axis) and plotted the distribution profiles of fluorescence intensity at pronuclear meeting and NEB by adding the signal at each point along the normalized length of the AP axis. To eliminate variation arising from curvature of the cortex at the cell poles, we analyzed only a segment from 0.2 to 0.8 EL. For each zygote, relative distribution of NMY-2–GFP along the AP axis was calculated as the fraction of total cortical signal at each point along the axis. Data presented in Fig. S1 A are mean values for each genotype/RNAi condition. A *t* test (two-tailed, assuming unequal variance) was used to compare values between genotypes at each axial position. To simultaneously visualize cortical NMY-2–GFP and centrosomes (Fig. S1 B), we collected a cortical fluorescence z-series and a DIC image of the NCC every 10 s. Fluorescence z-series corresponding to each time point were projected as a sum, and stacks were normalized for EL. Each stack was cropped to a median 50% of egg width, and then the reslice command was used to generate a three-dimensional kymograph. This was flattened by projecting the average (mean) of all slices, thus reducing the AP axis to a row of pixels and generating a kymograph that showed change in the AP intensity profile over time. All kymographs were autoadjusted for brightness and contrast, aligned with reference to the time of NEB, and averaged. Corresponding DIC stacks were likewise normalized for EL, and the centrosomes were marked at each 10-s time point; these marked stacks were used to generate kymographs using the same method as used for fluorescence.

Particle tracking

To quantify the movements of actomyosin aggregates, we measured NMY-2–GFP displacements occurring at time scales ranging from 0.25 to 16 s. Fig. 5 (C and D) shows the trajectories of all cortical NMY-2–GFP aggregates in a wild-type zygote imaged over 60 s using 1- and 12-s time scales. The trajectory of each aggregate is described by a single track; sampling the aggregates' displacements at time intervals of 1 s (time scale = 1 s) will yield a set of displacements (in this case, up to 59; shown in Fig. 5 C). Sampling at a longer time scale (12 s) yields a smaller number of displacements of more widely distributed magnitude (Fig. 5 D). Importantly, sampling at this longer time scale reveals directional trends in aggregate movement that may not be apparent at shorter time scales. Note that from the same set of trajectories, a different set of displacements over a 12-s interval would be obtained by shifting the initial sampling time point. Therefore, when measuring displacements over a time scale longer than the acquisiton frame rate, the most complete description is obtained by sampling all possible overlapping time frames in each image sequence. Thus, we extracted all displacements at a given time scale and analyzed frequency distributions of displacement size and direction.

Zygotes were observed using DIC optics until the time of pronuclear meeting; the objective was then focused on the upper cortex, and images of a single focal plane were collected at intervals of 0.25–1 s beginning 30 s after pronuclear meeting. After recording for 30–60 s, we determined the direction of NCC rotation and confirmed that the cell successfully divided and that its daughters reentered interphase. Although we could not simultaneously record movements of NMY-2–GFP aggregates and the NCC, we found that during the longer 60-s period of data collection, the NCC in wild-type zygotes moves anteriorly a mean distance of 12 ± 2% of EL and rotates through a mean angle of 28 ± 14° (*n* = 25). In Gα-depleted zygotes, the NCC moves 5.5 ± 2% of EL toward the anterior and rotates through 14 ± 13° (*n* = 16). In let-99(or513ts) zygotes, the NCC moves 1 ± 2% of EL toward the anterior and changes its direction of rotation four to five times (*n* = 16).

Image sequences were opened using ImageJ, background was subtracted, and the stack was rotated to align the zygote horizontally with anterior to the left before saving as a series of 8-bit TIFF images. Further image processing and analysis were performed using IDL (Research Systems, Inc.). NMY-2–GFP aggregates were tracked as described previously (Marcus et al., 1996; Margineantu et al., 2000; Knowles et al., 2002) The first image of the sequence was imported and digitally filtered using a Gaussian filter of 11-pixel (0.7 μm) diameter. A set of features was defined (Fig. 5, A and B) corresponding to the brightest regions distinguishable through the Gaussian filter; most of these were too faint to be discerned by eye and were removed by selecting for brightness. The remaining set of features was overlaid on the original image to confirm identity with observed NMY-2–GFP aggregates. The features identified were compiled into a time-dependent trajectory that linked features corresponding to the same aggregates in successive frames. Trajectories were plotted on the x and y coordinates to visualize aggregate displacements (Fig. 5, C and D). Histograms of aggregate displacements as a function of time scale were constructed from the aggregate trajectories. Distributions of aggregate displacements were analyzed at the time scale of 12 s. This choice represented a compromise between the objectives of detecting biologically driven behaviors (increasingly prominent with increasing time scale) and maintaining a representative dataset: at longer time scales, considerably fewer data points were available from a subset of recordings that lasted 30 s.

MSDs were calculated as a function of the time scale τ from the aggregate trajectories according to the method outlined by Margineantu et al. (2000). The two orthogonal projections of the MSD—parallel and perpendicular to the AP axis—are given by the formulas $\langle [x(t)-x(t+\tau)]^2 \rangle$ and $\langle [y(t)-y(t+\tau)]^2 \rangle$, respectively. The angle brackets indicate that the x- and y-component MSDs are averaged over all aggregates within a designated spatial region (i.e., an octant) and over all possible starting times (*t*) of the image frame sequence.

Online supplemental material

Fig. S1 quantitatively shows the spatial distribution of cortical NMY-2–GFP in wild-type, *goa-1(RNAi);gpa-16(RNAi)*, and *let-99(or513*ts*)* at the times of pronuclear meeting and NEB (A). It also shows for each genotype a time course of averaged NMY-2–GFP intensity profile over the AP axis during 240 s before NEB together with a time course of centrosome positions in the same zygotes (B). Figs. S2–4 show histograms of NMY-2–GFP aggregate displacements at time scales of 4, 8, 12, and 16 s for wild type (Fig. S2), goa-1(−);gpa-16(−) (Fig. S3), and let-99(−) (Fig. S4). Videos show wild-type centration (Video 1), defective centration in *let-99*(−) and its suppression or enhancement after actomyosin manipulation (Videos 2–6), wild-type distribution of cortical NMY-2–GFP from pronuclear migration through cytokinesis (Video 7), and high speed image sequences used for particle tracking analysis of cortical NMY-2–GFP during centration in wild-type, goa-1(−);gpa-16(−), and let-99(−) zygotes (Videos 8–10). Online supplemental material is available at http://www.jcb.org/cgi/content/full/jcb.200703159/DC1.

References

Albertson, D.G. 1984. Formation of the first cleavage spindle in nematode embryos. *Dev. Biol.* 101:61–72.

Bellanger, J.-M., J.C. Carter, J.B. Phillips, C. Canard, B. Bowerman, and P. Gonzcy. 2007. ZYG-9, TAC-1 and ZYG-8 together ensure correct microtubule function throughout the cell cycle of *C. elegans* embryos. *J. Cell Sci.* 120:2963–2973.

Brenner, S. 1974. The genetics of *Caenorhabditis elegans*. *Genetics*. 77:71–94.

Bringmann, H., C.R. Cowan, J. Kong, and A.A. Hyman. 2007. LET-99, GOA-1/GPA-16, and GPR-1/2 are required for aster-positioned cytokinesis. *Curr. Biol.* 17:185–191.

Chen, S., and H.E. Hamm. 2006. DEP domains: more than just membrane anchors. *Dev. Cell*. 11:436–438.

Cheng, N.N., C.M. Kirby, and K.J. Kemphues. 1995. Control of cleavage spindle orientation in *Caenorhabditis elegans:* the role of the genes *par-2* and *par-3*. *Genetics*. 139:549–559.

Colombo, K., S.W. Grill, R.J. Kimple, F.S. Willard, D.P. Siderovsky, and P. Gönczy. 2003. Translation of polarity cues into asymmetric spindle positioning in *Caenorhabditis elegans* embryos. *Science*. 300:1957–1961.

Cowan, C.R., and A.A. Hyman. 2004. Asymmetric cell division in *C. elegans:* cortical polarity and spindle positioning. *Annu. Rev. Cell Dev. Biol.* 20:427–453.

Cuenca, A.A., A. Schetter, D. Aceto, K. Kemphues, and G. Seydoux. 2003. Polarization of the *C. elegans* zygote proceeds via distinct establishment and maintenance phases. *Development*. 130:1255–1265.

Encalada, S.E., P.R. Martin, J.B. Phillips, R. Lyczak, D.R. Hamill, K.A. Swan, and B. Bowerman. 2000. DNA replication defects delay cell division and disrupt cell polarity in early *Caenorhabditis elegans* embryos. *Dev. Biol.* 228:225–238.

Etemad-Moghadam, B., S. Guo, and K.J. Kemphues. 1995. Asymmetrically distributed PAR-3 protein contributes to cell polarity and spindle alignment in early *C. elegans* embryos. *Cell*. 83:743–752.

Euteneuer, U., and M. Schliwa. 1985. Evidence for an involvement of actin in the positioning and motility of centrosomes. *J. Cell Biol.* 101:96–103.

Goldstein, B., and S.N. Hird. 1996. Specification of the anteroposterior axis in *Caenorhabditis elegans*. *Development*. 122:1467–1474.

Gotta, M., and J. Ahringer. 2001. Distinct roles for G∝ and Gβγ in regulating spindle position and orientation in *Caenorhabditis elegans* embryos. *Nat. Cell Biol.* 3:297–300.

Grill, S.W., and A.A. Hyman. 2005. Spindle positioning by cortical pulling forces. *Dev. Cell*. 8:461–465.

Grill, S.W., P. Gonczy, E.H. Stelzer, and A.A. Hyman. 2001. Polarity controls forces governing asymmetric spindle positioning in the *Caenorhabditis elegans* embryo. *Nature*. 409:630–633.

Grill, S.W., K. Kruse, and F. Julicher. 2005. Theory of mitotic spindle oscillations. *Phys. Rev. Lett.* 94:108104.

Guo, S., and K.J. Kemphues. 1996. A non-muscle myosin required for embryonic polarity in *Caenorhabditis elegans*. *Nature*. 382:455–458.

Hampoelz, B., and J.A. Knoblich. 2004. Heterotrimeric G proteins: new tricks for an old dog. *Cell*. 119:453–456.

Hill, D.P., and S. Strome. 1988. An analysis of the role of microfilaments in the establishment and maintenance of asymmetry in *Caenorhabditis elegans* zygotes. *Dev. Biol.* 125:75–84.

Hwang, E., J. Kusch, Y. Barral, and T.C. Huffaker. 2003. Spindle orientation in *Saccharomyces cerevisiae* depends on the transport of microtubule ends along polarized actin cables. *J. Cell Biol.* 161:483–488.

Hyman, A.A., and J.G. White. 1987. Determination of cell division axes in the early embryogenesis of *Caenorhabditis elegans*. *J. Cell Biol.* 105:2123–2135.

Kamath, R.S., A.G. Fraser, Y. Dong, G. Poulin, R. Durbin, M. Gotta, A. Kanapin, N. Le Bot, S. Moreno, M. Sohrmann, et al. 2003. Systematic functional analysis of the *Caenorhabditis elegans* genome using RNAi. *Nature*. 421:231–237.

Kemphues, K.J., J.R. Priess, D.G. Morton, and N.S. Cheng. 1988. Identification of genes required for cytoplasmic localization in early *C. elegans* embryos. *Cell*. 52:311–320.

Kimura, A., and S. Onami. 2005. Computer simulations and image processing reveal length-dependent pulling force as the primary mechanism for *C. elegans* male pronuclear migration. *Dev. Cell*. 8:765–775.

Knowles, M.K., M.G. Guenza, R.A. Capaldi, and A.H. Marcus. 2002. Cytoskeletal-assisted dynamics of the mitochondrial reticulum in living cells. *Proc. Natl. Acad. Sci. USA*. 99:14772–14777.

Koelle, M.R., and H.R. Horvitz. 1996. EGL-10 regulates G protein signaling in the *C. elegans* nervous system and shares a conserved domain with many mammalian proteins. *Cell*. 84:115–125.

Kozlowski, C., M. Srayko, and F. Nedelec. 2007. Cortical microtubule contacts position the spindle in *C. elegans* embryos. *Cell*. 129:499–510.

Labbe, J.C., E.K. McCarthy, and B. Goldstein. 2004. The forces that position a mitotic spindle asymmetrically are tethered until after the time of spindle assembly. *J. Cell Biol.* 167:245–256.

Marcus, A.H., B. Lin, and S.A. Rice. 1996. Self-diffusion in dilute quasi-two-dimensional hard sphere suspensions: evanescent wave light scattering and video microscopy studies. *Phys. Rev. E. Stat. Phys. Plasmas. Fluids Relat. Interdiscip. Topics*. 53:1765–1776.

Margineantu, D., R.A. Capaldi, and A.H. Marcus. 2000. Dynamics of the mitochondrial reticulum in live cells using Fourier imaging correlation spectroscopy and digital video microscopy. *Biophys. J.* 79:1833–1849.

Miller, K.G., and J.B. Rand. 2000. A role for RIC-8 (Synembryn) and GOA-1 (G(o)alpha) in regulating a subset of centrosome movements during early embryogenesis in *Caenorhabditis elegans. Genetics*. 156:1649–1660.

Motegi, F., and A. Sugimoto. 2006. Sequential functioning of the ECT-2 RhoGEF, RHO-1 and CDC-42 establishes cell polarity in *Caenorhabditis elegans* embryos. *Nat. Cell Biol.* 8:978–985.

Munro, E., J. Nance, and J.R. Priess. 2004. Cortical flows powered by asymmetrical contraction transport PAR proteins to establish and maintain anterior-posterior polarity in the early *C. elegans* embryo. *Dev. Cell*. 7:413–424.

Pecreaux, J., J.-C. Röper, K. Kruse, F. Jülicher, A.A. Hyman, S.W. Grill, and J. Howard. 2006. Spindle oscillations during asymmetric cell division require a threshold number of active cortical force generators. *Curr. Biol.* 16:2111–2122.

Piekny, A.J., and P.E. Mains. 2002. Rho-binding kinase LET-502 and myosin phosphatase MEL-11 regulate cytokinesis in the early *Caenorhabditis elegans* embryo. *J. Cell Sci.* 115:2271–2282.

Piekny, A.J., A. Wissmann, and P.E. Mains. 2000. Embryonic morphogenesis in *Caenorhabditis elegans* integrates the activity of LET-502 Rho-binding kinase, MEL-11 myosin phosphatase, DAF-2 insulin receptor and FEM-2 PP2c phosphatase. *Genetics*. 156:1671–1689.

Reinsch, S., and P. Gonczy. 1998. Mechanisms of nuclear positioning. *J. Cell Sci.* 111:2283–2295.

Rogers, S.L., U. Wiedemann, U. Hacker, C. Turck, and R.D. Vale. 2004. *Drosophila* RhoGEF2 associates with MT plus ends in an EB1-dependent manner. *Curr. Biol.* 14:1827–1833.

Rose, L.S., and K. Kemphues. 1998. The *let-99* gene is required for proper spindle orientation during cleavage of the *C. elegans* embryo. *Development*. 125:1337–1346.

Rosenblatt, J., L.P. Cramer, B. Baum, and K.M. McGee. 2004. Myosin II-dependent cortical movement is required for centrosome separation and positioning during mitotic spindle assembly. *Cell*. 117:361–372.

Severson, A.F., and B. Bowerman. 2003. Myosin and the PAR proteins polarize microfilament-dependent forces that shape and position mitotic spindles in *Caenorhabditis elegans*. *J. Cell Biol.* 161:21–26.

Severson, A.F., D.L. Baillie, and B. Bowerman. 2002. A formin homology protein and a profilin are required for cytokinesis and Arp-2/3-independent assembly of cortical microfilaments in *C. elegans. Curr. Biol.* 12:2066–2075.

Shelton, C.A., J.C. Carter, G.C. Ellis, and B. Bowerman. 1999. The nonmuscle myosin regulatory light chain *mlc-4* is required for cytokinesis, anterior-posterior polarity, and body morphology during *Caenorhabditis elegans* embryogenesis. *J. Cell Biol.* 146:439–451.

Sugimoto, N., N. Takuwa, H. Okamoto, S. Sakurada, and Y. Takuwa. 2003. Inhibitory and stimulatory regulation of rac and cell motility by the $G_{12/13}$-rho and G_i pathways integrated downstream of a single G protein-coupled sphingosine-1-phosphate receptor isoform. *Mol. Cell. Biol.* 23:1534–1545.

Tsou, M.F., A. Hayashi, L.R. DeBella, G. McGrath, and L.S. Rose. 2002. LET-99 determines spindle position and is asymmetrically enriched in response to PAR polarity cues in *C. elegans* embryos. *Development*. 129:4469–4481.

Tsou, M.F., A. Hayashi, and L.S. Rose. 2003. LET-99 opposes G∝/GPR signaling to generate asymmetry for spindle positioning in response to PAR and MES-1/SRC-1 signaling. *Development*. 130:5717–5730.